Quantitative Microwave Backscatter Measurements from the Ocean Surface Using Digital Marine Radar Images

C. P. GOMMENGINGER, N. P. WARD, G. J. FISHER, I. S. ROBINSON, AND S. R. BOXALL

School of Ocean and Earth Sciences, Southampton Oceanography Centre, Southampton, United Kingdom

(Manuscript received 11 May 1998, in final form 28 June 1999)

ABSTRACT

The capabilities for quantitative measurements of the ocean backscatter at low grazing angles of a conventional low-budget X-band marine radar associated with a commercial digital capture board are investigated. Details are given of the external and internal calibration methods designed to determine the system's transfer function. This work reveals that the accurate system transfer function can be determined only by calibrating the composite system in one single step. Results of an absolute calibration attempt using buoy-based corner reflectors in very calm weather conditions are presented. The dynamic range is deduced and found to span over a 50-dB range well suited to describe the ocean backscatter coefficient values expected at low grazing angles. The analysis of the overall error budget and system stability provides a theoretical estimate of the system's relative radiometric resolution. The marine radar system is found to produce backscatter coefficient images with a relative error typically of the order of 1 dB. When averaging over several antenna rotations, the error reduces further down to 0.6 dB, where it compares favorably with the performance of traditional research radar systems. It is concluded that despite the inexpensive nature of these instruments, marine radar systems represent a tool that is effective in routinely providing reliable quantitative measurements of the sea surface roughness, which may serve to complement the synoptic views offered commonly by satellite or airborne radars.

1. Introduction

In recent years, microwave remote sensing has become an area of great interest for both academic and operational oceanographers. Airborne and satellite-based microwave radars have now clearly proven their ability to provide high-resolution images of sea surface roughness variabilities such as those associated with swell waves, surface active slicks, or the presence of internal waves or bathymetric features (Vesecky and Stewart 1982). However, when routine operational use over a particular area is required, these highly sophisticated radar systems are prohibitively expensive to run and offer only a limited temporal coverage and poor measurement repetivity.

In comparison, shore or ship-based conventional marine radars have only occasionally been used for scientific applications, as they are generally considered unsuitable as investigative tools for research. Until recently, access to marine radar backscatter data for scientific purposes was difficult, involving the lengthy processing of photographs of radar video display screens (Watson and Robinson 1990). The advent in recent years of digital capture board technology has enabled marine radars to produce high-resolution digital images in real time. Among the few examples of scientific applications, most are concerned with the extraction of directional ocean wave spectra (Young et al. 1985; Hirakuchi and Ikeno 1990; Henschel et al. 1994), although applications to oil spill detection (Tennyson 1988; Atanassov et al. 1991) and wave refraction patterns imaging (Boalch and McManus 1989) can also be found.

To date, however, the large majority of these studies has made use only of the qualitative information in marine radar data. Some investigations at the Naval Research Laboratory (NRL) have used calibrated high-resolution U.S. Navy marine radars to examine the nature of ocean backscatter at low grazing angles (Trizna 1991; Trizna and Carlson 1996; Trizna 1997), but these offer little indication of the performances of a typical low-budget nautical radar system as a means for routine quantitative measurements of the sea surface roughness.

In this paper, we examine the capabilities of a typical low-budget navigational radar attached to a commercially available digital data capture board. Although this work focuses on the calibration and performance assessment of one particular system, it is hoped that the results can be representative of the capabilities for quantitative ocean backscatter measurements of similar low-budget nautical radar systems. After a succinct descrip-

Corresponding author address: C. P. Gommenginger, Department of Oceanography, Southampton Oceanography Centre, European Way, Southampton SO14 3ZH, United Kingdom.
E-mail: c.gommenginger@soc.soton.ac.uk

TABLE 1. Marine radar system technical characteristics and calculated and measured absolute calibration scaling factor K.

Pulse setting	Pulse length (μs)	PRR (Hz)	Peak power (kW)	Radial footprint (m)	K calculated (dB)	K measured (dB)
Short pulse	0.08	2400	7.0	12	31.6	31.3
Medium pulse	0.3	1200	10.0	45	33.1	35.8
Long pulse	1	600	11.5	150	33.7	36.8

tion of the data collection procedure, the paper reviews the parameters involved in the normalization of the radar images. Particular attention is given to the method conceived to obtain the accurate determination of the system transfer function with a brief history of early unsuccessful attempts. An effort toward absolute calibration of the system is reported and enables the assessment of the system's dynamic range. The data quality issue is examined to produce an evaluation of the radiometric error in the system's estimate of the ocean backscatter coefficient. The performance of the system as a quantitative backscatter measuring device is finally put into perspective in relation to other microwave radar systems and user requirements for the study of oceanographic processes.

2. Instrumentation

The radar system consists of a conventional marine radar coupled to a digital capture board based on a personal computer (PC). The capture board intercepts radar backscatter signals at the output of the radar amplifier and digitizes and stores them as binary image files on the PC. A detailed description of the radar system can be found in Robinson et al. (1999, manuscript submitted to *J. Atmos. Oceanic Technol.*).

a. The X-band marine radar

The radar is an X-band Racal Decca marine radar fitted with a 1.8-m linear antenna rotating with a 2.4-s period. The horizontal beamwidth at half-power is approximately 1°, producing a 10-m-wide antenna footprint at 500 m. The emitted X-band frequency of 9.4 GHz corresponds to a wavelength of 3.2 cm. As for most marine radars, the polarization is horizontal (HH). The microwave energy is emitted in the form of pulses of varying lengths—short (0.08 μs), medium (0.3 μs), or long (1 μs)—which produce nominal antenna footprints 12, 45, or 150 m long, respectively, in the radial direction. Both the pulse peak power and pulse repetition rate (PRR) are determined by the pulse length setting (Table 1). On reception, the radar signal is log-amplified and displayed on the radar video display unit (VDU).

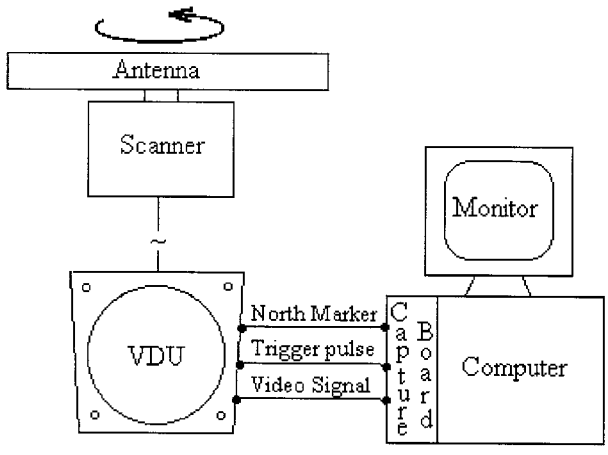

FIG. 1. Composite radar and data capture board setup.

b. Data capture board

The data capture board is PC based and synchronized with the radar via three links (Fig. 1). The north marker pulse provides the radar heading reference point, the trigger pulse marks each pulse emitted by the magnetron, and the video signal consists of the log-amplified returns from the sea surface. This backscatter signal is extracted by the capture board at the output of the log-amplifier and is unaffected by any signal processing occurring downstream (e.g., rain/sea clutter filtering, sensitivity time control) designed to improve the display of the signal on the VDU.

Various adjustable parameters control the data capture and determine the properties of the digital radar image. The image's spatial coverage in azimuth can be set to up to 180°. The image's resolution in azimuth is determined by the number of independent ''looks'' (or successive echoes returned from the sea surface) averaged by the capture board per pixel in azimuth. In order to reduce speckle, the number of looks is maximized generally to match the image resolution in azimuth with the antenna's physical horizontal beamwidth. Hence, for a 2.4-s antenna rotation period, a 1° beamwidth, and the PRR values given in Table 1, the number of looks for short, medium, and long pulse settings is equal typically to 16, 8, and 4 pulses, respectively.

The integrated multilook backscatter signal is then sampled at a rate of 20, 10, or 5 MHz, resulting in an image pixel resolution in range equal to 7.5, 15, or 30 m, respectively. The backscatter signal is digitized to 8 bits (256 gray levels) and stored on the PC. The buffer size of the capture board is limited to 512 bytes, each byte corresponding to one pixel in range. Hence, for a sampling rate of 10 MHz, the image's spatial coverage in range is limited to 7680 m (4.2 nmi).

The data capture board also permits images of the same area to be collected over several antenna rotations.

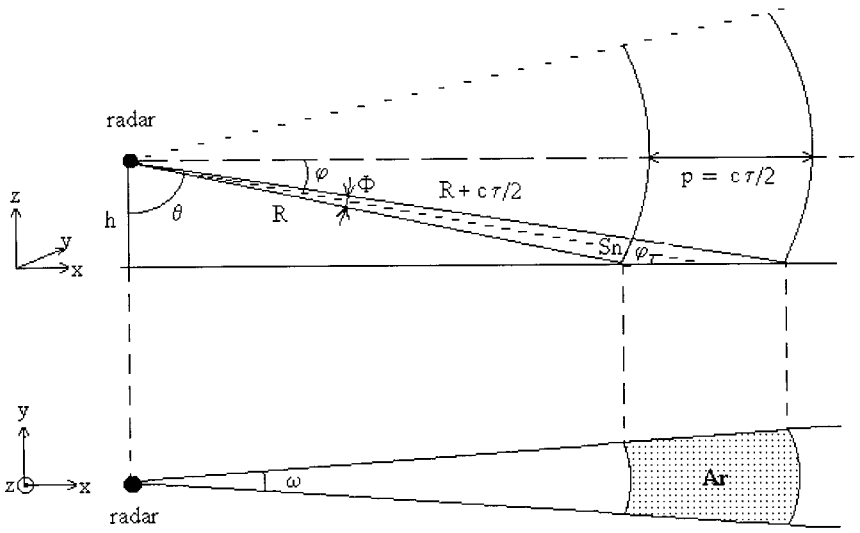

FIG. 2. Geometry of the pulsed radar antenna footprint and sea clutter resolution cell: R is the slant range of the range resolution cell's nearest point, φ is the grazing angle, and ϕ is the pulse-limited vertical beamwidth of the radar beam.

The production of such time series allows the pixel-to-pixel averaging of sequential images into an average backscatter image for which the radar backscatter signal-to-noise ratio is much improved. Similarly, images of higher-order statistical moments can also be computed.

3. Image normalization

The radar backscatter intensity in each pixel represents the power received at the antenna from the sea area illuminated by the antenna at that range. For a unit area of sea surface, the ratio of the scattered power to the incident power defines the surface's backscatter coefficient, also known as the normalized radar cross section (NRCS), usually expressed in decibels. Although the scattering mechanisms responsible for microwave radar backscatter at near-horizontal incidence angles are not well understood, the scattered power is known to increase with increasing wind and sea conditions, and the NRCS can thus be taken as a measure of the sea surface roughness.

a. Radar equation

The power received at the antenna P_r is related to the NRCS σ^0 of a target by the radar equation (Ulaby et al. 1982)

$$P_r = \frac{P_t g(\theta, \phi) A_e \sigma^0 A_r}{(4\pi)^2 R^4}, \tag{1}$$

where R is the slant range (m) of the target, P_t the transmitted power (W), $g(\theta, \phi)$ the antenna gain pattern in azimuth (θ) and elevation (ϕ), A_e the effective aperture of the antenna (m^2), and A_r the physical area of the target (m^2). For highly directional marine radar antennas, the gain $g(\theta, \phi)$ can be approximated by the maximum antenna gain, $G = g(0, 0)$. In the present case, G is taken equal to 28 dB, following the manufacturer's technical specifications. The antenna's effective aperture A_e is related to the antenna's physical area A and the antenna efficiency η by $A_e = \eta A$, and represents the performance of the antenna in reception. The antenna's effective aperture can be related to the maximum gain of the antenna by $A_e = G\lambda^2/4\pi$, where λ is the wavelength of the radar radiation (m). Thus, replacing A_e in (1) leads to the NRCS in decibels:

$$\begin{aligned}\sigma^0 \text{ (dB)} &= 10 \log_{10}\sigma^0 \\ &= 10 \log_{10}P_r + 10 \log_{10}R^4 - 10 \log_{10}A_r \\ &\quad - 10 \log_{10}K,\end{aligned} \tag{2}$$

where the NRCS is a function of received power, target range, physical area of the target, and a scaling factor K characteristic of the properties of the magnetron and antenna, which can be evaluated as $K = P_t G^2 \lambda^2/(4\pi)^3$.

b. Sea clutter area A_{rs}

For distributed targets, the physical area of the target A_r is equivalent to the size of the antenna beam footprint on the sea surface. At high angles of incidence, the footprint of the pulsed radar beam is limited in azimuth by the horizontal beamwidth of the antenna ω and is limited in range by the temporal length of the radiated pulse τ (Fig. 2). The equivalent spatial length of the radar pulse p is given in meters by $p = c\tau/2$, where c is the speed of light ($c = 3 \times 10^8$ m s^{-1}) and τ is the radar pulse length (s). Assuming a flat earth approximation, Fig. 2 yields the rigorous expression for the

pulse-limited vertical beamwidth Φ of the radar beam (rad) as

$$\Phi = \cos^{-1}\left(\frac{h}{R + p}\right) - \cos^{-1}\left(\frac{h}{R}\right), \quad (3)$$

where h is the height of the radar antenna (m). Hence, the solid angle of the pulsed radar beam Ω (rad^2) is given by $\Omega = \Phi\omega$, and the area normal to the incident radiation is $S_n = R^2\Omega$ (m^2). Given the expression for the grazing angle, $\varphi = \sin^{-1}(h/R)$ in radians, the sea clutter area A_{rs} (m^2) can be written as

$$A_{rs} = \frac{S_n}{\sin\varphi} = \frac{R^2\Phi\omega}{\sin\varphi}. \quad (4)$$

For near-grazing angles (Φ small), (4) is equivalent to the classical expression of the clutter cell limited by pulse length (Nathanson 1969):

$$A_{rs} \approx \frac{R\omega c\tau}{2\cos\varphi}. \quad (5)$$

c. Received power P_r

The signal intensity in the images is related to the received power P_r at the antenna by the radar system transfer function. This relationship includes transmission losses in the radar's various components, the radar logarithmic amplification, and the digital capture board transfer function. The determination of the system transfer function constitutes the major effort in the normalization of the radar images and is examined in the next section.

4. Radar system transfer function

a. External calibration approach

1) FORMULATION

Most modern marine radars are fitted with logarithmic amplifiers designed to increase the dynamic range of the instrument, improve the detectability of targets at far ranges, and reduce the risk of saturation at close ranges. To first approximation, the amplification function may be assumed to be perfectly logarithmic. The relation between received power and intensity is then expressed on a logarithmic scale as a linear function:

$$X = A\log_{10}P_r + B, \quad (6)$$

where X is the image intensity in digital numbers (DNs) and A and B are two constants defining the amplification function. From (2) and (6), we can write

$$10\log_{10}P_r = 10\log_{10}(\sigma^0 A_r) + 10\log_{10}K - 10\log_{10}R^4; \quad (7)$$

$$10\log_{10}P_r = 10\left(\frac{X - B}{A}\right). \quad (8)$$

After equating (7) and (8), we obtain

$$10\log_{10}R^4 = CX + D, \quad (9)$$

with

$$C = -\frac{10}{A} \quad \text{and} \quad (10)$$

$$D = \frac{10B}{A} + 10\log_{10}(\sigma^0 A_r) + 10\log_{10}(K). \quad (11)$$

The numerical values of C and D can then be determined experimentally by plotting $10\log_{10}R^4$ against the echo intensity X for targets of known radar cross section, $\sigma_t = \sigma_t^0 A_{rt}$, located at different ranges. These empirically determined coefficients will be referred to hereafter as C_t and D_t to indicate that they were obtained from measurements over calibrated point targets. Analytically these coefficients are equal to

$$C_t = -\frac{10}{A}; \quad (12)$$

$$D_t = \frac{10B}{A} + 10\log_{10}(\sigma_t) + 10\log_{10}K. \quad (13)$$

Hence, substituting (8) in the expression for the NRCS [(2)] and given the expressions for C_t and D_t [(12) and (13)], the NRCS of the sea surface σ_s^0 can be represented finally in decibels as a function of the pixel intensity X:

$$\sigma_s^0\,(\text{dB}) = -C_tX - D_t + 10\log_{10}(\sigma_t) + 10\log_{10}R^4 - 10\log_{10}A_{rs}, \quad (14)$$

where C_t and D_t are the coefficients determined empirically from calibrated point targets, σ_t is the radar cross section of the calibrated point target (m^2), R is the slant range of the pixel (m), and A_{rs} is the sea surface area (m^2) illuminated by the radar antenna at that range. It should be noted that the traditional R^{-3} dependence of σ_s^0 on range is included implicitly given the quasilinear dependence of A_{rs} on R at low grazing angles. Hence, the empirical determination of the coefficients C_t and D_t enables the definition of the end-to-end transfer function of the radar system.

2) PRELIMINARY RESULTS AND VALIDATION

The coefficients C_t and D_t were determined experimentally from radar images collected in Christchurch Bay off the south coast of the United Kingdom. In this area, numerous navigational buoys fitted with radar reflectors are located at various ranges and azimuths from the radar position, and allowed us to plot $10\log_{10}R^4$ versus X with reasonable accuracy. The radar reflectors on all buoys were 16-in. octahedral Speckter reflectors with a reported radar cross section $\sigma_t = \sigma_t^0 A_{rt}$ equal to 10 m^2 (J. Simmons 1994, personal communication). The reflector echo intensities X were measured in images averaged over 16 antenna rotations. The coefficients C_t and D_t at medium pulse were determined by least square

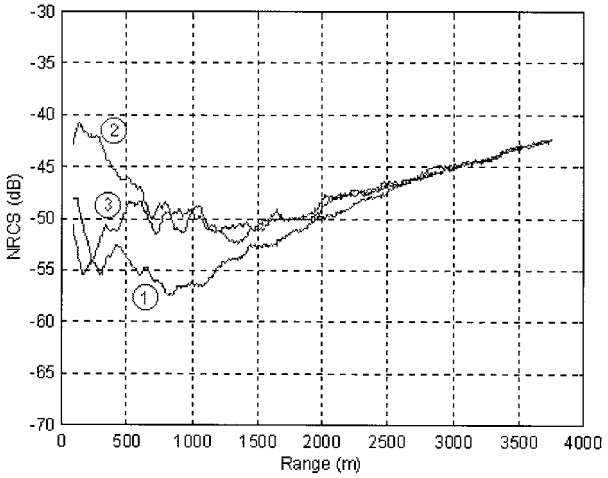

FIG. 3. Calculated NRCS using the external calibration results applied to radial transects in three images of the same area in different environmental conditions: (1) $U10 \sim 5$ m s^{-1}, (2) $U10 \sim 13$ m s^{-1}, and (3) $U10 \sim 8$ m s^{-1}.

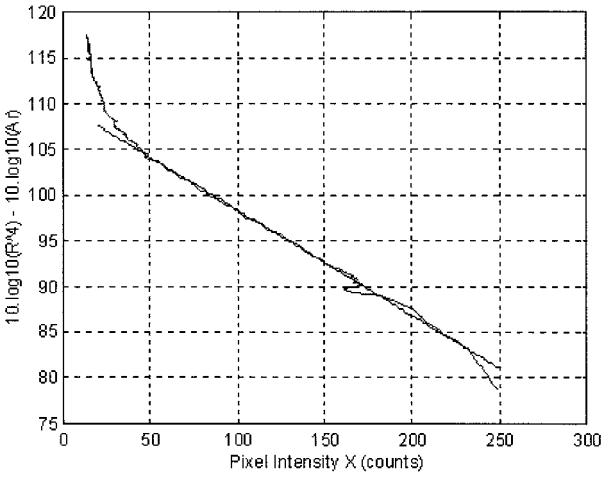

FIG. 4. Experimental evidence of nonlogarithmic behavior of the radar amplifier at low and high pixel intensities. The discrepancy around $X = 170$ relates to an oceanographic feature in the image and should be ignored.

fitting of a linear function to the data points and were found equal to -0.206 and 170, with 95% confidence intervals of ± 0.03 and ± 5, respectively. The system's end-to-end transfer function (14) may thus be rewritten for the medium pulse length case as

$$\sigma_s^0 \text{ (dB)} = 0.206X + 10 \log_{10} R^4 - 10 \log_{10} A_{rs} - 160. \quad (15)$$

Validation was sought by applying these preliminary results to a set of radar images collected from a coastal location over the same area on three occasions characterized by different wind and sea conditions. Issues relating to the estimation of the error in the computed NRCS will be addressed in section 6. The surface roughness could be assumed to be spatially uniform over chosen parts of the images, so that the NRCS outside the breaking zone was expected to be either constant or decreasing with range because of the possible shadowing of the sea surface by wave crests at very small grazing angles.

Representative transects of the calibrated images are presented in Fig. 3. At close range, within 1000 m, the NRCS shows a clear increase with wind speed, thus marking the increase in surface roughness, with inshore wave breaking further enhancing the NRCS at high winds. Beyond 1000 m, however, the NRCS unexpectedly, is seen to increase steadily with range regardless of environmental conditions. This trend could not be related to any effective increase in sea surface roughness in this region, so an instrumental effect was implied. Further tests showed that this behavior coincides with the onset of low levels of received power, as suggested by the steady increase becoming discernible at closer range for lower wind–sea conditions. It was thus inferred that the assumption of a perfect logarithmic amplification does not apply at low power levels, where the amplifier output voltage tends toward the constant voltage associated with the receiver noise.

This nonlogarithmic behavior of the amplifier at low power levels was further confirmed by data obtained from other sites. Figure 4 shows the quantity $10 \log_{10}(R^4) - 10 \log_{10} A_{rs}$ plotted against intensity X for every pixel of a radar image radial transect obtained over an area assumed uniformly rough. If the amplification were perfectly logarithmic, the plot would be linear with X [see (15)], but the data are seen clearly to deviate from the linear form at both high and low intensities. The hypothesis of a perfect logarithmic function therefore introduces discrepancies for low- and high-power returns, which result in computed NRCS values that are over- and underestimated, respectively.

b. Internal calibration approach

1) HISTORY

In light of the external calibration approach's shortcomings, an internal calibration procedure was undertaken to define as accurately as possible the system transfer function at low and high received power levels. A first experimental method consisting of a two-step procedure was carried out initially, in which the radar and capture board were calibrated separately and the respective transfer functions were combined subsequently. This method offered the advantage of being easy to implement in practice but eventually yielded results contradictory to the external calibration results. Full details of this experiment thus are not presented here but can be found in Gommenginger (1997).

Although this experiment failed to produce the desired improved system transfer function, several observations of relevance for later work were made. First, the range of input voltages accepted by the data capture

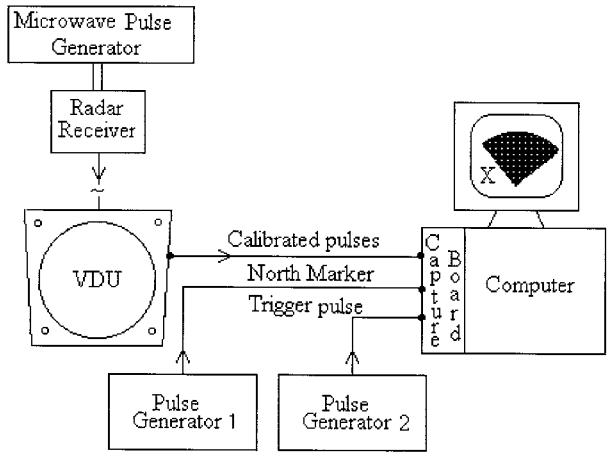

FIG. 5. Experimental setup for one-step internal calibration setup of the composite radar system.

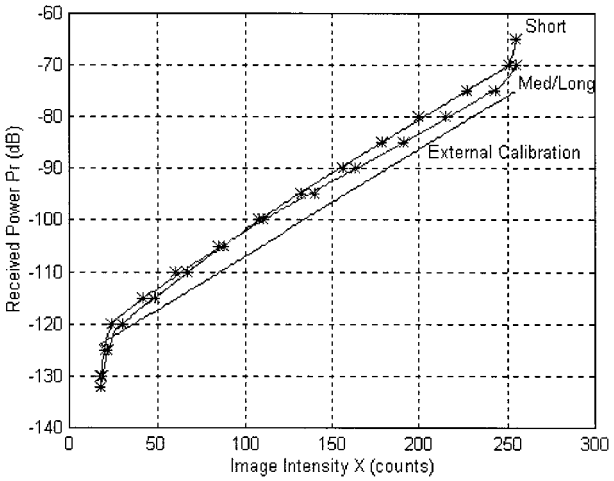

FIG. 6. Qualitative comparison between the one-step and the external calibrations.

board was found to correspond to the lower section of the range of output voltages generated by the radar. The system thus is better suited to measuring low-power backscatter. It follows that the dynamic range of the composite system is governed by the noise level of the marine radar and the saturation level of the data capture board.

Second, the medium and long pulse settings were found to share the same amplification function and to differ only in the peak power P_t and the duration of the emitted pulse. Hence, the system transfer function relating the received power P_r to the pixel intensity X needs to be determined only for short and medium–long settings, while the absolute calibration coefficient K needs to be determined for all three settings. The medium–long setting also revealed additional amplification for low-power echoes, which implies differences in the system's detection performance in the different pulse settings.

2) ONE-STEP CALIBRATION

The one-step method was disregarded initially following technical difficulties with implementation. The calibration of the radar system requires the injection of calibrated microwave pulses into the radar receiver and implies the disconnection of the transmitting unit and antenna rotating plate, as well as the removal of the antenna. The radar consequently is unable to produce the north marker and the trigger pulse necessary to drive the data capture board. To resolve this problem, two AC/DC pulse generators were introduced to simulate a pseudo–north marker and a pseudotrigger pulse signal that were then injected into the data capture board (Fig. 5). Microwave pulses of variable power were produced using a calibrated pulsed X-band microwave generator. After synchronizing the microwave pulse generator and the pseudotrigger pulse generator, the digital data capture board was set to collect artificial ''images'' of the calibrated microwave pulses for incremented power levels.

The resulting empirical transfer functions relating the received power in decibels, P_r, to the image intensity X for short and medium–long settings are shown in Fig. 6 and compared with the external calibration result for a medium pulse. At intermediate intensities, there is good qualitative agreement between the slopes of the external calibration function and the one-step calibration function for medium pulse. At lower image intensities, the one-step amplification function clearly diverges from the ideal logarithmic form for intensities around 50, which compare favorably with the experimental observations in Fig. 4. Hence, the expression of NRCS in decibels in (2) can be rewritten as

$$\sigma^0\ (\text{dB}) = f_{\text{s,m/l}}(X) + 10\ \log_{10}R^4 - 10\ \log_{10}A_{\text{rs}} - 10\ \log_{10}K, \tag{16}$$

with f_{s} and $f_{\text{m/l}}$ the amplification functions for short and medium–long pulses, respectively, obtained by least square fitting a polynomial function to the data points shown in Fig. 6; R the slant range (m); A_{rs} the sea patch area; and K the scaling factor characteristic of the transmitting/receiving properties of the magnetron and antenna.

The one-step calibration results were validated by calculating the NRCS for the same dataset as used previously to verify the external calibration. Again, the issues relating to errors in the computed NRCS and to the stability of the radar system are discussed in section 6. The coefficient K was taken from the manufacturer's technical specifications (K = 33.1 dB in the medium pulse setting), and the results are shown in Fig. 7. The sharp NRCS decrease within 1000 m with increasing range is again related to differences in surface roughness in the nearshore area for different wind conditions. Beyond 1000 m, the NRCS over regions of uniform surface

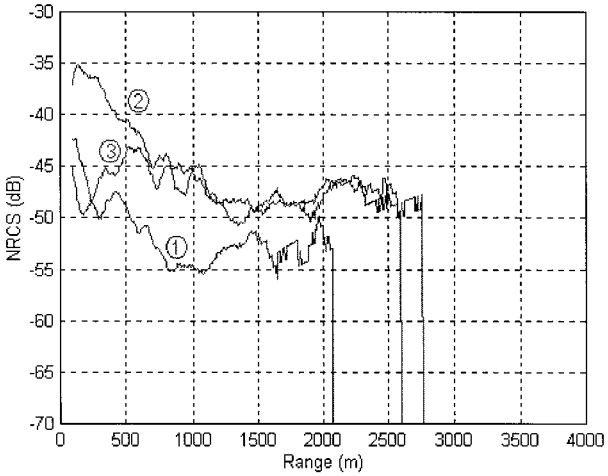

FIG. 7. Calculated NRCS using the one-step calibration results applied to the same dataset as used in Fig. 3.

roughness varies little with range and thus confirms the validity of the one-step calibration results. The system transfer function also defines implicitly the system's dynamic range and enables the identification of pixels displaying receiver noise and saturation signals. These pixels could then be assigned an arbitrary NRCS value (−70 dB in the case of receiver noise pixels in Fig. 7) and could be ignored subsequently in later processing. Further analysis of the system's dynamic range is presented in section 7.

5. Absolute calibration

The aim of the absolute calibration is to define the scaling factor K found in the radar equation (2), which relates the NRCS of a target to the intensity of its echo in a digital image. The determination of K is essential if the performances of the marine radar system as a quantitative NRCS measuring device are to be compared with more conventional research radars. So far, the scaling factor was calculated from the technical specifications provided by the radar manufacturer. But as these values are only indicative and may not represent reliably the capabilities of the current system, an experiment using calibrated point targets was devised to estimate the true scaling factor K for all pulse length settings.

The practical implementation of an absolute calibration is difficult because of the high sensitivity of the NRCS to the orientation of the target relative to the radar wave and because the measured target echo includes interference from multiple reflection and parasitic signals. The need for absolute measurements for marine radars is confined generally to research and development projects carried out by radar manufacturers to improve the radar's performances as a navigational aid. In order to minimize the risk of measurement error, such calibration experiments take place usually at specially designed sites featuring arrays of mast-based radar reflectors located at sea. Unfortunately, no opportunity for access to such facilities arose during this study. Instead, it was possible to make better use of the buoy-mounted corner reflectors used previously for the external calibration.

a. Multiple scattering

Measuring NRCS for targets raised above the sea surface is different from measuring the ocean backscatter coefficient. The radar equation given in (1) is valid only for point targets located in free space. The presence of the air–sea interface between the radar and the target allows for multiple scattering whereby the energy travels not only by the direct path but also by paths that include reflection from the sea surface between the radar and the target. In the case of a perfectly smooth surface and a horizontally polarized X-band radar wave, the magnitude of the reflected component to the backscatter can be of the same order as that of the direct component. Under these particular conditions, the contribution to the received power due to multiple scattering can be estimated and a new expression for the received power can be found as (Skolnik 1980)

$$P_r \approx \frac{4\pi P_t G^2 \sigma^0 A_r h_a^4 h_t^4}{\lambda^2 R^8}, \tag{17}$$

where, respectively, h_a and h_t are the heights of the radar antenna and the target above the mean sea level. It follows that the NRCS for a point target in the presence of a reflecting flat surface is given as

$$\sigma^0\ (\text{dB}) = 10\ \log_{10} P_r + 10\ \log_{10} R^8 - 10\ \log_{10} A_r - 10\ \log_{10} K', \tag{18}$$

where a new scaling coefficient K' is introduced as

$$K' = \frac{4\pi P_t G^2 (h_a h_t)^4 \lambda^2}{\lambda^2}. \tag{19}$$

From the expression for the original scaling factor K, the coefficient K' can be related to K by

$$K = \frac{K' \lambda^4}{(4\pi)^4 (h_a h_t)^4}. \tag{20}$$

b. Basis of a practical procedure for an absolute calibration

If an absolute calibration is to be achieved, the method for the external calibration described in section 4a must be adapted to allow for the multiple scattering discussed above. The assumption of a linear response now leads instead of (9), to

$$10\ \log_{10} R^8 = C'X + D'. \tag{21}$$

In principle, this enables C' and D' to be evaluated empirically as C_t' and D_t' from a series of measurements

of the signal echo from known targets (σ_t) at various ranges. Then, from (18) and (21), we can write

$$10 \log_{10} P_r = -C_t' X - D_t' + 10 \log_{10} \sigma_t + 10 \log_{10} K'. \quad (22)$$

But $10 \log_{10} P_r$ is described also by the internally derived calibration function $f_{s,m/l}(X)$. Thus, over the intermediate range in which the linear relationship between the received power in decibels, P_r and image intensity X is valid, we can say

$$f_{s,m/l}(X) = -C_t' X - D_t' + 10 \log_{10} \sigma_t + 10 \log_{10} K', \quad (23)$$

where for short pulse

$$f_s(X) = 0.223X - 125 \quad (24)$$

and for medium–long pulse

$$f_{m/l}(X) = 0.201X - 123. \quad (25)$$

Thus, C_t' can be assumed to be equal to the slope coefficient in (24) and (25) determined from the internal calibration, and all that remains is to determine D_{ts}', D_{tm}', and D_{tl}' by fitting (21) to measurements of known target echoes. Comparison of (23) with (24) and (25) yields expressions for the new scaling coefficient:

$$K_{short}' \text{ (dB)} = D_{ts}' - 10 \log_{10} \sigma_t - 125 \quad (26)$$

$$K_{med}' \text{ (dB)} = D_{tm}' - 10 \log_{10} \sigma_t - 123 \quad (27)$$

$$K_{long}' \text{ (dB)} = D_{tl}' - 10 \log_{10} \sigma_t - 123 \quad (28)$$

from which the original scaling factor K can be derived using (20).

c. Experimental results

Despite the obvious uncertainty associated with the motion of the buoys, the measurement errors were minimized by carrying out the experiment in very calm wind and sea conditions, thus reducing the pitch-and-roll motion of the buoys and limiting the contribution to the backscatter from the surrounding sea surface. The radar image spatial resolution was optimized to 7.5 m for the accurate measurement of the radar reflectors' sharp echoes intensities. For each target, a time series of 250 echo intensity measurements was obtained at each pulse setting and was submitted subsequently to statistical analysis.

It was noted from the distorted shape of the buoys' echoes that the radar receiver presented a low-filter-type response in which a delay is introduced in the time it takes for strong echoes to reach their nominal intensity. The rise time was found to be of the same order as the duration of the medium pulse and therefore was particularly detrimental to the measurement of target echo intensity in short pulse images. The temporal characteristic of the receiver response was estimated from radial transects in the artificial images obtained during the one-step internal calibration. Unfortunately, the maximum 20-MHz sampling rate used in these images proved inadequate to determine the time characteristic of the receiver accurately enough. As a result, only an approximate correction could be applied to the buoy intensities, and it is thought that a pulse-dependent bias may have been introduced at this stage that could question the validity of the empirical K values derived for different pulse settings from these measurements.

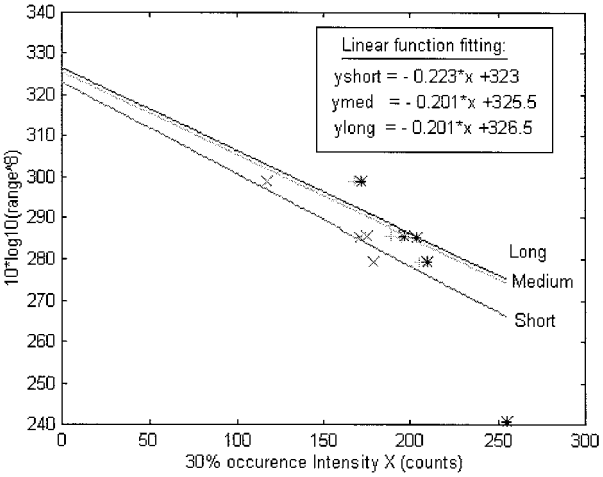

FIG. 8. Upper 30% echo intensity versus range for buoy-based radar reflectors. The slopes of the straight lines are preset from the one-step internal calibration results, and only the offset is determined by least square fitting to the empirical points for the calculation of D_t'. The outlier point at $X = 255$ corresponds to the saturation of the system for the nearest buoy and should be disregarded.

After correction of the echo intensities, the histograms for each time series were produced. The intensity associated with the 10 m^2 radar cross section (RCS) was identified by comparing our results with RCS statistics reported by Trinity House Lighthouse Service for this type of buoy-based radar reflectors. In their latest study (Ward and Vennings 1989), the performance of the Speckter radar reflectors was expressed in statistical terms for various buoy tilt angles. The 16-in. octahedral Speckter radar reflectors were found to behave well, and RCS statistics reported echoes larger or equal to 10 m^2 for 30% of the time for tilt angles between 0° and 10° from the vertical. In the very calm conditions encountered during our experiment, the buoy motion was assumed to belong to this range of inclinations. The intensity corresponding to the upper 30% of all echo occurrences was therefore determined for each buoy and associated with a 10 m^2 radar cross section. The range R and the 30% intensity $X_{30\%}$ of the radar reflectors were plotted as $10 \log_{10} R^8$ against intensity $X_{30\%}$ in Fig. 8. The intensity of the closest buoy echo unfortunately reached the system saturation level on all pulse lengths and could not be used in the linear function fitting. The offset D_t' was determined by least square fitting of the data points with a linear function of predetermined slope C_t' obtained from the one-step internal calibration functions at intermediate intensities expressed in (24) and

(25). The coefficient D_t' was found equal to 323, 325.5, and 326.5 for short, medium, and long pulses respectively. Following the calculation of the intermediate scaling factor K' from (26) to (28), the original scaling factor K was calculated using (19) for a radar height h_a of 7 m and a reflector height h_t of 3 m above mean sea level. This resulted in values of K equal to 31.3, 35.8, and 36.8 dB for short, medium, and long pulses.

These experimental results are compared in Table 1 with values of K calculated from the manufacturer's technical specifications for the maximum antenna gain (28 dB) and from laboratory measurements of the emitted power for each pulse setting. The numerical values of the empirically derived scaling factor K are in reasonably good agreement with the calculated values and indicate that the nominal antenna gain figure given by the manufacturer is a realistic estimate of the system's performances. However, given the uncertainty in the echo intensity correction factor for different pulse lengths, these experimental results are not sufficiently reliable to serve as a basis for the analysis of the radar's dynamic range capabilities on different pulse settings. Hence, it was deemed safer to perform the absolute calibration of images and the assessment of the system's NRCS using the calculated values of K. Thus, the final expression of the NRCS in decibels as a function of pixel intensity X (DN) at a range R (m) is

for short pulse:

$$\sigma^0\ (\text{dB}) = f_s(X) + 10\log_{10}R^4 - 10\log_{10}A_r - 31.6 \quad (29)$$

for medium pulse:

$$\sigma^0\ (\text{dB}) = f_{m/l}(X) + 10\log_{10}R^4 - 10\log_{10}A_r - 33.1 \quad (30)$$

for long pulse:

$$\sigma^0\ (\text{dB}) = f_{m/l}(X) + 10\log_{10}R^4 - 10\log_{10}A_r - 33.7, \quad (31)$$

where A_{rs} is the sea clutter area illuminated by the antenna as defined by (4), f_s and $f_{m/l}$ are the radar system amplification functions found during the internal calibration of the system for short and medium–long pulse settings, and the last term is the absolute calibration scaling factor calculated from laboratory measurements of the emitted power and the manufacturer's technical specification of the maximum antenna gain.

6. Error analysis

The NRCS of the sea surface at a given pixel is a function of many variables. The most important sources of error were identified as originating from the pixel intensity X (including the received power error linked to instrumental noise and the stability of the system), the transmitted power P_t, the pixel range R, and the radar antenna height h. Hence, the NRCS can be rewritten as

$$\sigma^0\ (\text{dB}) = W(X, P_t, R, h). \quad (32)$$

The NRCS measurement error of the radar system was estimated theoretically, as there was no opportunity for repeatable measurements over a static rough surface. Since the absolute error attached to the scaling factor K cannot be estimated easily, only the relative error was investigated at this stage. The estimation of this error will be rounded up systematically whenever required in order to achieve an evaluation of the maximum total relative error to be expected in the data.

a. Errors types

Measurement errors can be divided into systematic or random errors. Systematic errors are caused by incorrect methods of measurement and always bias the results in a particular direction. Usually this type of error does not affect the internal consistency of the measurements, but it becomes critical when comparing measurements with results from other experiments. Random errors are due to unavoidable interference during the measurements and are governed generally by Gaussian statistics. In contrast to systematic errors, random errors can be minimized by averaging over many realizations.

b. Error in pixel intensity

The error in the pixel intensity consists of the error in the received power related to the system noise and stability and to the digitization error introduced during the experimental determination of the instrument transfer function. The high accuracy of the microwave pulse generator used during the internal calibration experiment was found to result in a maximum digitization error less than 1 DN in the artificial images.

The error in the received power was identified as the main source of error in the NRCS, as it consists mostly of the system receiver noise. Receiver noise is a random error related to the thermal agitation of electrons in the instrument, and its statistical characteristics are related directly to the noise temperature of the receiver (Wheeler 1963). The thermal noise characteristics of the present system could be determined experimentally given the ability of the data capture board to collect radar images without prior power transmission. In the absence of transmitted pulses, the signals collected at the amplifier consist of the receiver noise plus the ambient microwave noise. At X-band frequencies and in the absence of other interfering systems in the vicinity, the natural level of microwave energy can be considered negligible in comparison with the instrumental noise. When other systems are present, the disruption of the data is generally sufficiently perceptible to ensure these data are rejected from the analysis.

Experimental measurements of the thermal noise

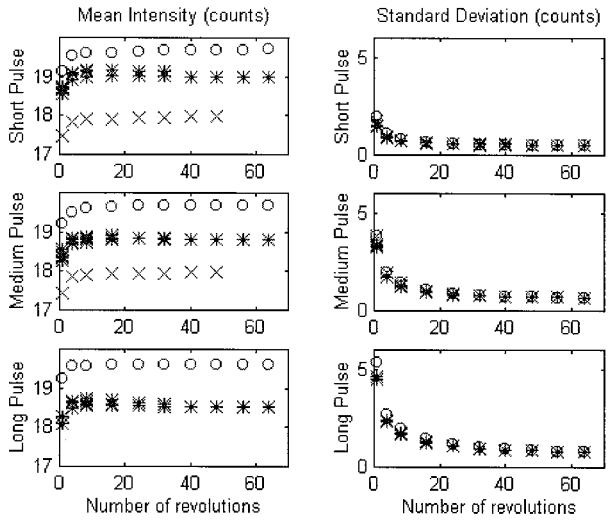

FIG. 9. Mean and standard deviation of the receiver noise in DN for a variable number of images averaged and three ambient temperatures: × = 12°C, + = 15°C, and ○ = 17°C.

were carried out on several occasions characterized by different environmental conditions to examine the stability of the system with temperature. On each occasion, a time series of 64 ''blind'' images was collected for all three pulse settings. For each time series, the average and standard deviation images were then produced for a variable number of antenna revolutions. The mean value in the average and standard deviation images was calculated by averaging over the whole image. The results for three different ambient temperatures are presented in Fig. 9 for all three pulse settings. The mean and standard deviation of the receiver noise are expressed in digital numbers between 0 and 255.

The mean receiver noise was found to be largely independent of pulse length setting and the number of revolutions but clearly dependent on temperature. The 5°C temperature difference between the datasets plotted as ''×'' and ''○'' in Fig. 9 correspond to a 1.5-count increase in the mean receiver intensity. Thus, the mean receiver noise should in principle be measured for every data capture session but can be assumed safely to be less than 25 counts in most environmental conditions.

The receiver noise standard deviation was found independent of temperature but showed a clear $1/N^{1/2}$ dependence on N, the number of images averaged, in accordance with Gaussian statistics. The variability of the receiver noise appeared larger for long and medium pulse settings, presumably because of the smaller number of independent looks on longer pulse settings. The receiver noise error was then digitized by rounding up to the nearest DN value for a range of N values. The total error in pixel intensity S_x was derived by combining the digitization error and the receiver noise error. The results are summarized in Table 2 for all pulse length settings and a range of N values.

TABLE 2. Pixel intensity error in DN on different pulse settings and a variable number of images averaged.

Pulse setting	Number of rotations N	Noise error S_x in DN
Short	$N < 4$	3
	$N \geq 4$	2
Medium	$N < 4$	5
	$4 \leq N < 16$	3
	$N \geq 16$	2
Long	$N < 4$	7
	$4 \leq N < 8$	4
	$8 \leq N < 24$	3
	$N \geq 24$	2

c. Error in emitted power

The transmitted power P_t is affected by a random error linked to the thermal agitation in the magnetron and fluctuations in the power supply. The random pulse-to-pulse fluctuations of the peak power is one of the parameters used to characterize the quality of the magnetron. In the present case, the pulse-to-pulse error is specified by the manufacturer (English Electronic Valves, Chelmsford, United Kingdom) to be less than ±10% of the mean peak power over a wide range of temperature and humidity conditions.

Adopting the rigorous assumption that the manufacturer's confidence limit represents one standard deviation of the emitted power pulse population, it follows from the laws of random errors that the error in the emitted power for images in which n_i number of independent looks are integrated per pixel in azimuth is

$$S_{n_i} = \frac{S_1}{n_i^{1/2}} = \frac{0.1\overline{P_t}}{n_i^{1/2}}, \tag{33}$$

where S_1 is the standard deviation of the single pulse population and $\overline{P_t}$ is the mean emitted power (W). Similarly, the error in emitted power for radar images collected with n_i number of looks and averaged over N antenna rotations becomes

$$S_{P_t} = \frac{S_{n_i}}{N^{1/2}} = \frac{0.1\overline{P_t}}{(Nn_i)^{1/2}}. \tag{34}$$

The error S_{P_t} in the peak power in radar images can then be calculated for all pulse settings and for a variable number of antenna revolutions N from the values of $\overline{P_t}$ given in Table 1 and the nominal number of independent looks n_i associated with each pulse setting.

d. Error in range

The error in the range of a given feature is a random error of very small magnitude determined in principle by the accuracy in measuring the time delay between the pulse emission and the reception of the echo. With the digitization of the returned echoes, however, small variations in range can result in a feature appearing alternately on two adjacent pixels. The error in range in a radar image is then a random error with a magnitude

determined by the sampling rate used for the digitization. Hence, for short-pulse images collected with a 20-MHz sampling rate, for example, the maximum error in range S_R is 7.5 m.

e. Error in antenna height

The error in the antenna height is a systematic error that biases the results for a given site in a particular direction. It is accountable for the discrepancies between results obtained from different radar locations. In coastal sites, the height of the antenna with respect to the mean sea level is determined whenever possible by direct measurement or visual estimate, taking into account any tidal elevation of the sea surface. When an accurate visual estimation is not available, the antenna height can be obtained from the nearest altitude reading on 1:50 000 Ordnance Survey maps. For much of the U.K. coastline, the Ordnance Survey will guarantee levels to an accuracy of the order of about 10 m (Ordnance Survey 1998, personal communication). Thus, the largest error in antenna height S_h is of the order of 10 m, where high locations such as cliffs are used.

7. Radiometric resolution and dynamic range

a. Radiometric resolution

The error analysis established that the total relative NRCS error consists of random errors in the pixel intensity X, the emitted peak power P_t, and the range R, as well as a systematic error in the height h of the antenna. Following (32) and the laws of error combination (Boas 1983), the relative NRCS error can be written as

$$\delta\sigma^0_{\text{relative}} = [(\delta W_X)^2 + (\delta W_{P_t})^2 + (\delta W_R)^2]^{1/2} + \delta W_h, \quad (35)$$

where δW_X, δW_{P_t}, δW_R, and δW_h are the relative errors expressed in decibels associated with pixel intensity, emitted power, range, and antenna height, respectively. The relative error in decibels for each variable is calculated from (32) and from the standard deviation of the variable. For example, the relative error in pixel intensity δW_X expressed in decibels reads

$$\delta W_X = |W(\overline{X}, \overline{P_t}, \overline{R}, \overline{h}) - W(\overline{X} + S_x, \overline{P_t}, \overline{R}, \overline{h})|, \quad (36)$$

where the overlined symbols indicate the mean value of the variable and S_X is the pixel intensity standard deviation expressed in DN.

From (35) and (32) it follows that the total relative error is a function of range, pixel intensity, antenna height, pulse setting, and the number of images averaged N. Closer examination of the dependence of the individual errors δW_X, δW_{P_t}, δW_R, and δW_h on these parameters leads to some simplifications. The rapid decay of δW_R and δW_h with range, for example, can be generalized easily by estimating the total error in three image range gates: smaller than 200 m, between 200 and 400 m, and larger than 400 m. Similarly, the dependence on antenna height can be resolved by assimilating the error δW_h to the maximum error as calculated for a range of antenna heights varying between 5 and 100 m above mean sea level.

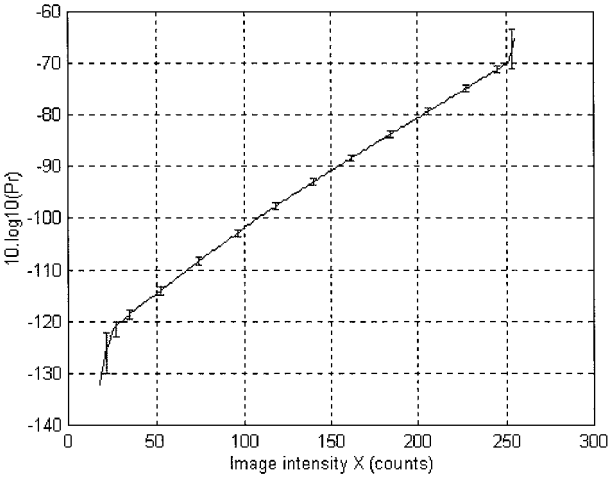

FIG. 10. NRCS relative error in decibels due to pixel intensity error shown as error bars for a pixel intensity error of $S_x = 3$ DN on a short pulse setting.

The dependence of the total error on pixel intensity through δW_X can also be removed by considering the variation of the error δW_X, with intensity. Figure 10 represents δW_X in the form of error bars for a pixel intensity standard deviation S_X of 3 DN. The error appears small and stable throughout the intermediate range of intensities but becomes very large rapidly at low and high intensities. Hence, it is clear that the high slope of the system transfer function at both extremes of the intensity range renders these data unreliable and implies that these data should not be included in the quantitative interpretation of the NRCS. It is therefore possible to remove the dependence of the total error in NRCS on intensity by redefining the system's dynamic range as the interval of received power levels for which the error δW_X is stable. In terms of intensities, this range corresponds to X values between 30 and 245. The error δW_X can then be represented by the maximum error in that range for given values of S_X. After simplification, the total relative error in NRCS then finally can be estimated from (35) as a function of pulse setting, range gate, and the number of averaged images as presented in Table 3.

b. Dynamic range

The radiometric dynamic range is defined as the range of NRCS values measurable with the present system. In principle, its lower and upper limits are determined, respectively, by the system's minimum detectable signal (MDS) related to the marine radar noise level and the saturation level of the data capture board. In the present case, however, the high NRCS error found in the pre-

TABLE 3. Radiometric resolution on different pulse settings, range gates, and a variable number of images averaged.

Pulse setting	Number of rotations N	Maximum error $\delta W_{\text{relative}}$ (dB) $R < 200$ m	Maximum error $\delta W_{\text{relative}}$ (dB) $R \geq 200$ m	Maximum error $\delta W_{\text{relative}}$ (dB) $R \geq 400$ m
Short	$N < 4$	1.5	1	0.9
	$N \geq 4$	1.3	0.8	0.6
Medium	$N < 4$	1.7	1.4	1.3
	$4 \leq N < 16$	1.3	0.9	0.8
	$N \geq 16$	1.2	0.7	0.6
Long	$N < 4$	2.1	1.9	1.8
	$4 \leq N < 8$	1.4	1.2	1.1
	$8 \leq N < 24$	1.2	0.9	0.8
	$N \geq 24$	1.1	0.7	0.6

vious section at high and low power levels has called for a redefinition of the system's dynamic range to the intensity interval between 30 and 245, where the major error δW_X is reduced (Fig. 10). Thus, the lower limit of the dynamic range (or MDS equivalent NRCS) is calculated for each pulse setting by introducing $X = 30$ DN in the normalization equations [(29)–(31)], while the system saturation level (or saturation-equivalent NRCS) is obtained by taking $X = 245$ DN in the same equations. The MDS and saturation-equivalent NRCS are shown in Fig. 11 for all pulse settings.

8. Discussion

a. Calibration methods

For the first time, the radiometric performance of a conventional low-budget marine radar attached to a digital capture board has been investigated. The internal calibration, implemented via a two-step and a one-step method highlighted the importance of treating the composite radar system as a whole to describe the system transfer function with sufficient accuracy for low and high backscatter signals. The one-step calibration method provided results in good agreement with experimental evidence obtained from external measurements on calibrated targets.

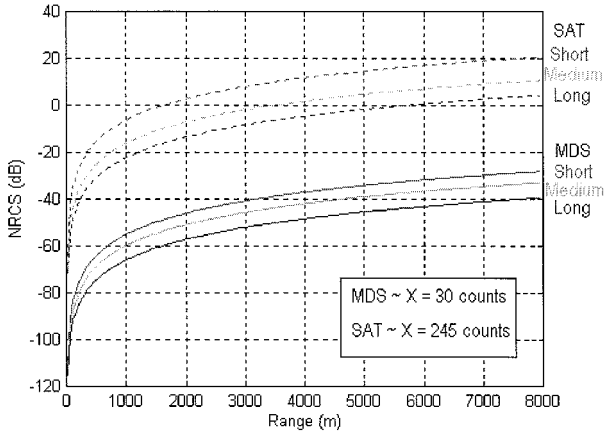

FIG. 11. Dynamic range defined by the NRCS interval between the minimum detectable signal (solid lines) and the saturation level (dotted lines) for different pulse settings. At 7 m s^{-1} wind speed, the low grazing ocean NRCS at HH polarization is typically between -20 and -30 dB.

The experimental method for the absolute calibration is admittedly questionable, chiefly because of the use of unsteady buoy-based targets. The approach, however, did account for the possibility of multiple scattering, and buoy measurements were obtained statistically over several hundred samples in very calm conditions for which both the buoys' motion and the contribution to the backscatter from the surrounding sea surface were minimal. Although the empirical results showed reasonable agreement with calculated values of the scaling coefficient K, the lack of accuracy in measuring the receiver's low-filter temporal characteristics represents a serious problem, as the derived correction factor is likely to include a pulse-length-dependent bias that could misrepresent the performance of the system on different pulse settings. For these reasons, the system performances were evaluated using the more reliable scaling coefficients K calculated from laboratory measurements of the emitted power and the estimate of the nominal antenna gain suggested by the manufacturer.

b. Dynamic range

From the literature, the range of ocean NRCS measured by airborne and shipborne HH-polarized microwave systems at low grazing angles is reported to vary between -60 and -10 dB (Daley et al. 1971; Trizna 1985), while the typical ocean NRCS for a 7 m s^{-1} wind speed is of the order of -20 to -30 dB. The dynamic range of the marine radar system shown in Fig. 11 spans a 50-dB range, which covers easily these low ocean backscatter values. The widely recognized ability of marine radars to detect low-power echoes at far ranges seems to be further enhanced by the filtering and integrating achieved in the digital capture board. The processing of the returned pulses in the composite system thus results in a reduced signal-to-noise ratio and an extension of the marine radar's dynamic range toward lower NRCS values. Hence, this ability to measure low-power echoes makes the marine radar system a cheap and simple method to study quantitatively the ocean backscatter at near-horizontal incidence angles.

c. Radiometric resolution

The radiometric resolution of the system shown in Table 3 for various combinations of parameters is seen to improve significantly for ranges beyond 400 m, where it is found to be of the order of 1 dB. Hence, for typically sized radar images, this smaller error applies over more than 90% of the image area and therefore can be considered to represent the overall quality of the digital radar images.

For single-rotation images, the 0.9–1.8-dB error is clearly much poorer than that of traditional research radars, which can claim accuracies better than 0.5 dB (Vogelzang et al. 1992; Meadows and Wright 1994). Nevertheless, this error is better than 1 dB for a short pulse and is therefore of sufficient quality to image the most rapidly changing oceanographic features with reasonable accuracy. The marine radar system offers the additional facility of producing time series of 2D images that may be used to study the spatial and temporal evolution of the sea surface roughness distribution over any period of time, ranging from seconds to minutes to hours, in a manner inaccessible to satellite or airborne systems.

For stationary oceanographic processes, the radiometric resolution in the digital marine radar images can be improved significantly down to 0.6 dB by averaging over several antenna revolutions. On short pulse settings, such low relative errors can be achieved by averaging as few as four successive images. Hence, images from different sites and obtained under different environmental conditions can now be compared with confidence, and most oceanographic processes characterized by radar backscatter signatures over of a few decibels (surfactant slicks, bathymetry–current interactions, fronts, etc.) can be studied quantitatively in space and time with good accuracy using this type of instrument.

9. Conclusions

The performance of a low-budget composite marine radar and data capture board system has been established for the quantitative measurement of the ocean backscatter coefficient. The system's dynamic range was found well adapted for sea surface roughness measurements at low grazing angles, and its radiometric resolution was revealed of sufficient quality to enable accurate imaging of many oceanographic phenomena. Marine radar systems thus represent a simple and affordable technique to obtain high-resolution quantitative images of the sea surface roughness distribution over specific areas.

The good performance of marine radar systems at low grazing angles, their versatility in terms of temporal and spatial sampling technique, and their long-term deployment capabilities make these instruments ideal tools to complement satellite and airborne imaging radar data. The combination of quantitative sea surface roughness measurements from different types of radars should lead ultimately to a better description of oceanographic processes and a better understanding of the microwave backscatter mechanisms responsible for their radar signatures.

Acknowledgments. This work was supported by the Commission of the European Communities under a Human Capital and Mobility Award ERBCHBICT930388.

REFERENCES

Atanassov, V., L. Mladenov, R. Rangelov, and A. Savchenko, 1991: Observation of oil slicks on the sea surface by using marine navigation radar. *Proc. Int. Geoscience and Remote Sensing Symp.*, Helsinki, Finland, IEEE, 1323–1326.

Boalch, C. R., and J. McManus, 1989: Wave refraction pattern recognition off North Sea coasts using X-band radar. *Developments in Estuarine and Coastal Study Techniques*, J. McManus and M. Elliott, Eds., Olsen and Olsen, 79–84.

Boas, M. L., 1983: *Mathematical Methods in the Physical Sciences.* Wiley and Sons, 743 pp.

Daley, J. C., J. T. Ransone Jr., and J. A. Burkett, 1971: Radar sea return. JOSS I. NRL Rep. 7268, 49 pp.

Gommenginger, C. P., 1997: On the applicability of a conventional microwave marine radar system to quantitative measurements of the ocean surface roughness and oceanographic applications. Ph.D. dissertation, University of Southampton, 252 pp. [Available from University of Southampton, Highfield, Southampton SO17 1BJ, United Kingdom.]

Henschel, M. D., R. A. Paul, and B. M. Eid, 1994: Use of satellite synthetic aperture radar for operational measurement of ocean wave spectra. *Proc. ERIM Second Thematic Conf. on Remote Sensing for Marine and Coastal Environments*, New Orleans, LA, Environmental Research Institute of Michigan, 269–279.

Hirakuchi, H., and M. Ikeno, 1990: Wave direction measurement using marine X-band radar. *Proc. 22d Int. Conf. on Coastal Engineering*, Delft, Netherlands, Permanent International Association of Navigation Congresses and International Association for Hydraulic Research, 703–715.

Meadows, P. J., and P. A. Wright, 1994: *ERS-1* SAR analogue to digital converter saturation. *Proc. CEOS SAR Calibration Workshop*, Ann Arbor, MI, University of Michigan, 24–37.

Nathanson, F. E., 1969: *Radar Design Principles: Signal Processing and the Environment*, McGraw Hill, 626 pp.

Robinson, I. S., N. P. Ward, C. P. Gommenginger, and M. A., Tenorio-Gonzales, 2000: Coastal oceanography applications of digital image data from marine radar. *J. Atmos. Oceanic Technol.*, **17,** 721–735.

Skolnik, M. L., 1980: *Introduction to Radar Systems.* 2d ed. McGraw Hill, 581 pp.

Tennyson, E. J., 1988: Shipborne radar as an oil spill tracking tool: *Proc. 11th Arctic and Marine Oil Spill Program Tech. Seminar*, Vancouver, BC, Canada, Environment Canada, 385–390.

Trizna, D. B., 1985: Preliminary results of dual polarized radar sea scatter. *The Ocean Surface: Wave Breaking, Turbulent Mixing and Radio Probing*, Y. Toba and H. Mitsuyasu, Eds., D. Reidel, 297–302.

——, 1991: Statistics of low grazing angle radar sea scatter for moderate and fully developed ocean waves. *IEEE Trans. Antennas Propag.*, **39,** 1681–1690.

——, 1997: A model for Brewster angle damping and multipath effects on the microwave radar sea echo at low grazing angles. *IEEE Trans. Geosci. Remote Sens.*, **35,** 1232–1244.

——, and D. J. Carlson, 1996: Studies of dual polarized low grazing angle radar sea scatter in nearshore regions. *IEEE Trans. Geosci. Remote Sens.*, **34,** 747–756.

Ulaby, F. T., A. K. Fung, and R. K. Moore, 1982: *Radar Remote*

Sensing and Surface Scattering and Emission Theory. Vol. 2, *Microwave Remote Sensing: Active and Passive*, Addison-Wesley, 606 pp.

Vesecky, J. F., and R. H. Stewart, 1982: The observation of ocean surface phenomena using imagery from the SEASAT synthetic aperture radar: An assessment. *J. Geophys. Res.*, **87,** 3397–3430.

Vogelzang, J., H. C. Peters, G. P. Deloor, H. Pouwels, and G. J. Wensink, 1992: Sea bottom topography with X-band SLAR: The relation between radar imagery and bathymetry. *Int. J. Remote Sens.*, **13,** 1943–1958.

Ward, N., and D. A. S. Vennings, 1989: Radar reflectors trials, Annexe 6. Trinity House Lighthouse Service Development Rep. 12-1989/NW, Trinity House Lighthouse Service, East Cowes, Isle of Wight, United Kingdom, 16 pp.

Watson, G., and I. S. Robinson, 1990: A study of internal wave propagation in the Strait of Gibraltar using shore-based marine radar images. *J. Phys. Oceanogr.*, **20,** 374–395.

Wheeler, G. J., 1963: *Radar Fundamentals*. Prentice Hall, 105 pp.

Young, I. R., W. Rosenthal, and F. Ziemer, 1985: A three-dimensional analysis of marine radar images for the determination of ocean wave directionality and surface currents. *J. Geophys. Res.*, **90,** 1049–1059.